



Nanomolar inhibition of human OGA by 2-acetamido-2-deoxy-D-glucono-1,5-lactone semicarbazone derivatives



Mariann Kiss ^a, Erna Szabó ^b, Boglárka Bocskai ^a, Luu Thanh Sinh ^b,
 Conceicao Piedade Fernandes ^c, István Timári ^a, Joseph M. Hayes ^{c, **}, László Somsák ^{a, *},
 Teréz Barna ^{b, ***}

^a Department of Organic Chemistry, University of Debrecen, H-4002, POB 400, Debrecen, Hungary

^b Department of Genetics and Applied Microbiology, University of Debrecen, H-4002, POB 400, Debrecen, Hungary

^c School of Pharmacy & Biomedical Sciences, University of Central Lancashire, Preston, PR1 2HE, United Kingdom

ARTICLE INFO

Article history:

Received 12 March 2021

Received in revised form

11 June 2021

Accepted 12 June 2021

Available online 15 June 2021

Keywords:

hOGA

Expression

Inhibitor

Glyconolactone semicarbazone

QM/MM-PBSA

Halogen

Halogen–Hydrogen bond donor

ABSTRACT

O-GlcNAcylation is a dynamic post-translational modification mediated by O-linked β-N-acetylglucosamine transferase (OGT) and O-GlcNAc hydrolase (OGA), that adds or removes a single β-N-acetylglucosamine (GlcNAc) moiety to or from serine/threonine residues of nucleocytoplasmic and mitochondrial proteins, respectively. The perturbed homeostasis of O-GlcNAc cycling results in several pathological conditions. Human OGA is a promising therapeutic target in diseases where aberrantly low levels of O-GlcNAc are experienced, such as tauopathy in Alzheimer's disease. A new class of potent OGA inhibitors, 2-acetamido-2-deoxy-D-glucono-1,5-lactone (thio)semicarbazones, have been identified. Eight inhibitors were designed and synthesized in five steps starting from D-glucosamine and with 15–55% overall yields. A heterologous OGA expression protocol with strain selection and isolation has been optimized that resulted in stable, active and full length human OGA (hOGA) isomorph. Thermal denaturation kinetics of hOGA revealed environmental factors affecting hOGA stability. From kinetics experiments, the synthesized compounds proved to be efficient competitive inhibitors of hOGA with K_i -s in the range of ~30–250 nM and moderate selectivity with respect to lysosomal β-hexosaminidases. *In silico* studies consisting of Prime protein–ligand refinements, QM/MM optimizations and QM/MM-PBSA binding free energy calculations revealed the factors governing the observed potencies, and led to design of the most potent analogue 2-acetamido-2-deoxy-D-glucono-1,5-lactone 4-(2-naphthyl)-semicarbazone **6g** ($K_i = 36$ nM). The protocol employed has applications in future structure based inhibitor design targeting OGA.

© 2021 The Authors. Published by Elsevier Masson SAS. This is an open access article under the CC BY-NC-ND license (<http://creativecommons.org/licenses/by-nc-nd/4.0/>).

1. Introduction

O-GlcNAcylation has emerged as a major posttranslational modification (PTM) that indicates the energy, nutritional and stress status of the cell, and involves transfer of a single N-acetylglucosamine moiety from UDP-GlcNAc to a serine or threonine side chain of proteins [1]. The two most striking features of O-GlcNAcylation, which distinguish this PTM from N- and O-glycosylations are its

localisation and its dynamic nature. It is localized to cytosol, nucleus and mitochondria rather than the endoplasmic reticulum or Golgi apparatus [2]. Similar to phosphorylation, two opposing enzyme actions determine the level of O-GlcNAcylation of a protein: OGT (O-GlcNAc transferase), the transferase, which transfers the N-acetylglucosamine moiety and creates the β-glycosidic linkage between the protein and GlcNAc, and the hydrolase OGA (O-GlcNAcase), which cleaves the bond [3]. UDP-GlcNAc, produced by the hexosamine pathway, provides the GlcNAc moiety for OGT to transfer to the aliphatic hydroxyl groups of the proteins to be modified. This UDP-GlcNAc is the nutrient sensor of the cell and O-GlcNAcylation, in response to the hexosamine flux, modulates metabolism and affects numerous cellular processes such as transcription regulatory pathways, cell cycle progression, embryonic

* Corresponding author.

** Corresponding author.

*** Corresponding author.

E-mail addresses: jhayes@uclan.ac.uk (J.M. Hayes), somsak.laszlo@science.unideb.hu (L. Somsák), barna.terez@science.unideb.hu (T. Barna).

development, the regulation of the epigenome, respiration and proteosomal degradation [4–8]. *O*-GlcNAcylation does not only switch the biological function of key regulatory proteins on and off, but finely tunes their activities and interaction partners in the intracellular network. Imbalance in the GlcNAcylation cycle has been shown to manifest itself in diseases, where the hyperactivity of either OGA or OGT is observed. In nearly all cancers, an elevated level of *O*-GlcNAcylation was reported [9]. The trend is opposite in the brain, in multiple neurodegenerative diseases where decreased levels of *O*-GlcNAc modifications on numerous proteins have been reported, such as the proteins of the cytoskeleton [10]. The shift of homeostasis of *O*-GlcNAcylation to the increased hydrolysis of GlcNAc from the modified proteins is one of the main mechanisms contributing to neurodegeneration [11]. As a consequence of the complementary and competitive nature of phosphorylation and *O*-GlcNAcylation at many serine/threonine sites, low levels of *O*-GlcNAcylation leads to hyperphosphorylation of cytoskeleton proteins in the brain, including the microtubule protein tau. The hyperphosphorylated form of tau has been found in neurofibrillary tangles, characterized as tauopathy. An increase of *O*-GlcNAcylation levels by inhibiting the activity of OGA has significantly decreased the aggregation propensity of tau [12,13]. The considerable therapeutic relevance of dissecting the mechanism of *O*-GlcNAcylation, motivates biological studies, and design and synthesis of potent OGA inhibitors.

Human OGA (hOGA) is a neutral hexosaminidase and belongs to family 84 of glycoside hydrolases (GH84) [14]. The enzyme follows a two-step substrate-assisted mechanism, through a dissociative oxocarbenium ion-like transition state, resulting in the net retention of the anomeric configuration [15]. This mechanism is shared by the acidic *N*-acetylhexosaminidases, a member of GH20 [16]. In the GH84 family two neighbouring aspartates and in the GH20 enzymes, one aspartate and one glutamate, function as the key catalytic nucleophile and the acid/base residues [16–18]. There are specific human *N*-acetylhexosaminidases that reside in lysosomes and are expressed in several tissues, mostly as a mixture of two isoenzymes: *N*-acetylhexosaminidase A (HexA) and *N*-acetylhexosaminidase B (HexB) [19]. GH20 *N*-acetylhexosaminidases catalyse the hydrolysis of terminal, non-reducing *N*-acetyl- β -D-glucosamine and *N*-acetyl- β -D-galactosamine residues from proteoglycans [16,20]. Both isoforms appear in plasma and in synovial fluid and become elevated in inflammatory processes. In the synovial fluid of patients with osteoarthritis, HexA and HexB are released by chondrocytes into the extracellular compartment, mainly responsible for the degradation of glycosaminoglycans (GAG) [21,22]. Development of potent inhibitors against HexA and HexB are also highly relevant in studying the physiological role of these enzymes and their potential therapeutic applications.

PUGNAc (Phenyl Urethane of GlcNAc, Chart 1) was one of the first inhibitors of OGA [23] with a K_i value of around 50 nM, however, it is not selective, since it inhibits GH20 *N*-acetylhexosaminidases in a similar manner. The *N*-phenylcarbamate moiety

can form hydrogen bonds between the oxime nitrogen atom and catalytic site residues, and the phenyl moiety, which protrudes from the active site pocket, takes advantage of hydrophobic interactions with aromatic side chains [24]. 2-Acetamido-2-deoxy-D-gluconhydroximo-1,5-lactone (LOGNAc), which lacks the phenyl carbamate group, is an around 30 times less potent inhibitor [23], showing that this moiety makes an important contribution to binding. Several other inhibitors are known in the literature, mostly transition state analogue compounds (NAG-thiazoline, NButGT, Thiamet-G), glucoimidazoles (GlcNacstatins) and non-carbohydrate-based inhibitors have also been reported [25]. Surprisingly, there are only a few examples of PUGNAc analogues where the aromatic moiety is changed [26]. In addition, to the best of our knowledge, the effects of modifications of the urethane linker on OGA inhibition have not yet been studied.

Though PUGNAc is a well established OGA inhibitor, its synthesis has some drawbacks. The first eight-step synthetic route [27] (overall yield: 14%) included two critical steps: a) the incomplete and low yielding transformation of the starting compound in the oxidation step towards the hydroximo-1,5-lactone (50% with 35% unreacted starting material); b) a debenzylidenation with Na/NH₃. The scale-up of both transformations to multigram synthesis led to lower yields and involved inconvenient workup procedures [28]. In an improved six-step synthesis [28] (overall yield: 15%) the hydroximo-1,5-lactone was obtained in an 59% yield only, and for this step keeping the -40 °C temperature was crucial. At lower temperature the conversion was incomplete, while at higher temperature the 1,4-lactone oxime was formed.

With these preliminaries in mind we envisaged the synthesis of aryl substituted (thio)semicarbazones of 2-acetamido-2-deoxy-D-glucono-1,5-lactone (target compounds in Chart 1) whose preparation was expected to lack critical steps such as those for PUGNAc. Kinetics experiments were performed to determine the potencies for hOGA inhibition, as well as selectivity studies considering also *N*-acetylhexosaminidases. High level *in silico* calculations using quantum mechanics/molecular mechanics (QM/MM) methods were performed to understand the hOGA binding properties and relative inhibitory efficiencies of the compounds.

2. Results and discussion

2.1. Synthesis

A single representative of our target compounds (Chart 1, Ar = Ph, X = O) was located in the literature, therefore, the synthesis was based on the adaptation of this published procedure [29] (Table 1). The starting material 2-acetamido-3,4,6-tri-*O*-acetyl-2-deoxy-D-glucopyranose (**1**) was obtained by a known two-step procedure [30,31] from D-glucosamine hydrochloride. Compound **1** was then transformed by a 4-arylsenicarbazide (**2**, either commercial chemicals or obtained from the corresponding aromatic amines as described in the supporting material) in the presence of 10 mol% of

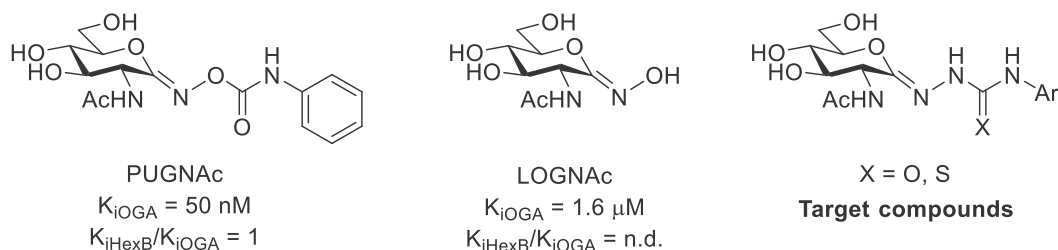


Chart 1. The structure of some OGA inhibitors and the target compounds of this study.

Table 1
Synthesis of the test compounds **6**.

Reagents and conditions: a) $\text{NH}_2\text{NH}_2 \cdot \text{H}_2\text{O}$, 1.0 equiv. pTsoH-H₂O, CHCl₃, reflux; b) $\text{NH}_2\text{NH}_2 \cdot \text{H}_2\text{O}$, 1.0 equiv. pTsoH-H₂O, CHCl₃, reflux; c) CrO_3 -pyridine, CHCl₃, reflux; d) CrO_3 -pyridine, CHCl₃, reflux; e) NH_3 , MeOH, reflux.

R	Products and yields (%)					
	3 + 4	Ratio ^a of 3 : 4	5	6	Overall yield of 6 from D-glucosamine	
a	CONHPh	90	5:1	83	79	49
b	CONH(<i>p</i> -MePh)	83	7:1	92	86	55
c	CONH(<i>p</i> -CF ₃ Ph)	81	5:1	26	87	15
d	CONH(<i>p</i> -OMePh)	87	7:3	86	83	52
e	CONH(<i>p</i> -ClPh)	77	4:1	78	74	37
f	CONH(1-naphthyl)	94	^b	64	83	41
g	CONH(2-naphthyl)	80	^b	93	75	46
h	CSNHPh	87 ^c	—	78	83	47

^a Determined from the ¹H NMR spectra of the worked-up reaction mixtures.

^b Formation of the open-chain products **4f** and **4g** was detected by TLC but due to signal overlaps and small amounts of these compounds the 3 : 4 ratio was not established.

^c Compound **3** formed as a single product.

p-toluenesulfonic acid as catalyst to get the *N*1-glycosyl semicarbazides **3**. In place of the originally proposed 1,2-dichloroethane the use of dichloromethane, chloroform and toluene was tested for this transformation. In toluene the solubility of the starting material was insufficient, while the reaction in boiling CH₂Cl₂ resulted in lower yields than in CHCl₃ at reflux temperature, therefore, the latter solvent was used in the reactions. With the semicarbazide derivatives **2a-g** the equilibrating open-chain tautomers **4a-g** were also observed in the ¹H NMR spectra, while the reaction with thiosemicarbazide **2h** was devoid of this product. No attempt was made to separate compounds **3** and **4**. The NMR spectra of these mixtures contained signals which were analogous to those obtained for pure **3a** and **4a** in the literature [29]. The β(D) configuration of compounds **3** followed from the large ³J_{H-1-H-2} couplings of 9–10 Hz (*c.f.* Experimental section). Oxidation of the mixtures containing **3** and **4** with CrO₃-pyridine complex gave good yields of the expected lactone semicarbazones **5a-g**. Regrettably, these oxidation conditions yielded complex reaction mixtures in case of the thio derivative **3h**. Several oxidizing agents were tested (I₂/NEt₃, PIDA, ICl/Cs₂CO₃) and finally MnO₂ proved to be efficient to furnish the required compound **5h**. The lactone semicarbazones **5** were *O*-deprotected by a solution of NH₃ in MeOH to result in the test compounds **6**. The overall yields of these five-step synthetic sequences to give target compounds **6** from D-glucosamine fell in the 15–55% range.

To verify the configuration of the C=N bond in compounds **6**, a Nuclear Overhauser Effect (NOE) based NMR approach was applied to **6c** (Fig. 1). The *E-Z* isomeric forms of compounds **6** are expected to be distinguished on the basis of NOE cross-peaks between the N(2)H and distinctive protons of the sugar part, since the maximum spatial distance which can provide an NOE signal is about 5 Å. First,

a 2D ¹H–¹³C HMBC spectrum [32] (Fig. S1) was recorded for the unambiguous assignment of N(2)H (9.8 ppm). Then a 2D ¹H–¹H EASY ROESY experiment [33] was performed, which is a powerful alternative of NOE measurements for small molecules. In the ¹H–¹H ROESY spectrum (Fig. S2), the N(2)H resonance provided NOE cross-peaks with the H(5') and O(6')H resonances (Fig. 1), which indicated the vicinity in space of these protons, and so, the presence of the *Z* isomeric form of compound **6c**. Since both the ¹H and ¹³C NMR spectra for the other compounds **6** closely resemble those of **6c**, one can safely conclude the presence of the *Z* isomer also in those compounds.

2.2. Heterologous expression of hOGA

A heterologous expression system for hOGA in *E. coli* was

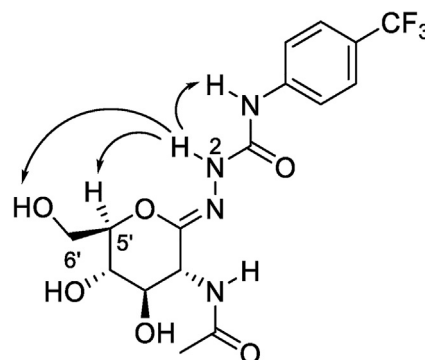


Fig. 1. Nuclear Overhauser Effects (NOEs) observed in compound **6c**.

established in order to gain soluble, active, full-length wild-type enzyme with considerable thermostability for the kinetic evaluation of the inhibitory potency of new inhibitors **6a-h** against hOGA. Bacteriophage T7 polymerase promoter based expression system such as BL21(DE3)/pET system was chosen for this purpose. The pET-28 based vector construct carrying the N-terminally His-tagged hOGA encoded gene was transformed into five *E. coli* BL21(DE3) strains and the cultivation conditions were optimized, as well as the environmental parameters of the downstream processes. The small scale expression trials of all the transformed BL21(DE3) strains carried out at 23 °C unravelled two main objectives to be solved in this expression system. Namely, the high tendency of the recombinant hOGA to form inclusion body aggregates during the protein production phase and the significant proteolytic degradation of the recombinant enzyme suffered *in vivo* and *in vitro* (Fig. 2). We did experience the latter phenomenon, despite all the strains used were deficient in two proteases, an outer membrane protease (ompT) and an ATP dependent protease (Lon), both of which have been reported as responsible for degradation of misfolded proteins and interference with production of some full-length recombinant proteins [34–36]. In this respect, the worst performing strain was BL21(DE3), where full length recombinant enzyme was hardly produced (Fig. 2). Beside the non-specific proteolysis, significant production of a 70 kDa long truncated hOGA fragment was observed with BL21 Star and pLysS strains referring to an existence of a sequence specific proteolytic cleavage site. This fragment bound to the affinity column and exhibited β -N-acetylglucosaminidase activity (see supporting material, Fig. S3). The size and activity of this comparatively stable hOGA fragment suggests the presence of caspase-3-like protease activity of *E. coli* cells that might be activated upon the overproduction of hOGA, causing a proteotoxic stress for the cell [37–40]. Two strains, RIPL and Rosetta, where the translation was optimized for genes that differ in codon usage from that of *E. coli* by carrying rare tRNA genes on plasmids, showed increased production of recombinant enzyme. However, only the Rosetta strain could increase the synthesis of the enzyme in the active, soluble form (Fig. 2). The productivity of the Star and pLysS strains was very similar with a relatively high yield of active hOGA compared to the aggregate form. This highlights the importance of the increased life-time of mRNA in Star and the very tight control of expression in pLysS (Fig. 2). However, Star and pLysS exhibited the highest site-specific proteolytic activity producing

the 70 kDa long hOGA fragment. Table S1 summarizes the β -N-acetylglucosaminidase activity of the cell lysates of the selected *E. coli* strain. It can be misleading to rely only on these results and rank the productivity of the strains according to these activity values. For instance, the BL21 (DE3) strain, which yielded the second highest β -N-acetylglucosaminidase activity, produced the lowest level of soluble, full-length recombinant enzyme. From all these observations it can be concluded that even though the strains have the same origin, they displayed different tolerance to the overproduction of misfolded protein, due to the activation of an extensive network of proteolytic housekeeping and regulating enzymes [41,42].

Since the Rosetta strain proved to be the best performing expression host, systematic cultivation parameters were optimized for this strain. The effect of temperature on the recombinant protein production was investigated below 30 °C, at three temperatures (16, 23 and 28 °C). The low protein concentrations in theory should decrease the partial folding and misfolding of proteins, thus, preventing the aggregation to inclusion body [43]. Decreasing the cultivation temperature only favoured full-length and active enzyme production at 23 °C. At lower temperature (16 °C), the misfolding of the human enzyme was accelerated and the chaperone systems of *E. coli* were not able to prevent the aggregate formation (see supplementary material, Fig. S4, Table S2).

The induction phase of the culture growth also influenced the yield of hOGA production. When the inducer was employed at later phase than the mid-exponential one (at OD_{600} 0.9 instead of 0.6), we could achieve 50% higher yield (expressed in total β -N-acetylglucosaminidase activity: 35 units for the mid-exponential phase induction and 53 units for the later phase induction in 250 ml cell culture) without compromising greater proteolytic degradation or formation of inclusion-body aggregates (Fig. S5).

All the optimized conditions were built in the final heterologous expression protocol for hOGA, in which aggregate formation of the overproduced enzyme was minimized and an efficient full-length, active hOGA production was ensured.

2.3. Stability studies on wild-type hOGA

The most important issue during the downstream processes was undoubtedly minimization of the action of *E. coli* proteases. Nevertheless, the identification of stabilizing and destabilizing factors involved in maintaining hOGA in its native state was also essential. Therefore, we carried out stability studies on hOGA by varying buffer compositions and we followed the heat-induced denaturation kinetics of the enzyme at 50 °C. The time-course of the enzyme residual activities was determined and the thermal denaturation kinetic constants (k_D) and the half-lives ($t_{1/2}$) were calculated. By increasing the ionic strength, the thermal denaturation rate of the enzyme increased too, as was detected in phosphate buffer upon increasing KCl concentration (Fig. S6a and Table S3). There was no significant difference in the rate of thermal denaturation of hOGA in the presence of either potassium or sodium cation (Fig. S6b and Table S3). Treating hOGA solution with reducing agents such as mercaptoethanol and DTT proved to be an important protective factor increasing the protein half-life by up to 25% (Table S3 and Fig. S7b). An even greater stabilizing effect was observed when phosphate buffer was supplemented with 15% glycerol to increase the enzyme half-life by 80% (Table S3). On the contrary, detergent Triton X-100 greatly destabilized hOGA native state and accelerated its thermal denaturation rate from $k_D = 0.05$ to $k_D = 0.17 \text{ min}^{-1}$, whereas the presence of Tween 20 proved to be an innocent factor in the structural disintegration of the enzyme (Fig. S7a and Table S3). The effect of the majority of environmental factors on thermal denaturation kinetics of hOGA could be

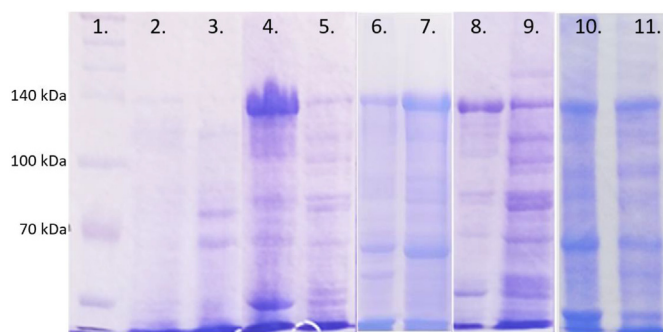


Fig. 2. Gel electrophoretic (8% SDS-PAGE) analysis of the soluble and insoluble fractions of the cell lysates produced by different *E. coli* BL21(DE3) strains grown at 23 °C, induced at mid-exponential phase with 0.4 mM IPTG and harvested at early stationary phase.

Lanes: 1. protein marker; 2. *E. coli* BL21(DE3) insoluble fraction; 3. *E. coli* BL21(DE3) soluble fraction; 4. *E. coli* BL21(DE3) RIPL insoluble fraction; 5. *E. coli* BL21(DE3) RIPL soluble fraction; 6. *E. coli* BL21(DE3) Rosetta insoluble fraction; 7. *E. coli* BL21(DE3) Rosetta soluble fraction; 8. *E. coli* BL21 Star (DE3) insoluble fraction; 9. *E. coli* BL21 Star (DE3) soluble fraction; 10. *E. coli* BL21(DE3) pLysS insoluble fraction; 11. *E. coli* BL21(DE3) pLysS soluble fraction.

modelled by a single-transient process between the native and unfolded states that obeys a first-order kinetics. When phosphate buffer alone was present, the heat denaturation of hOGA followed sigmoidal kinetics, which applies for an autocatalytic process (indicating the autocatalytic nature of the unfolding event). We did not investigate the mechanistic details further, however suggested explanation for the existence of cooperativity in domain conformational changes is discussed in the supplementary material.

We applied the stabilizing supplementations including the presence of reducing agent, Tween 20 and the preferable environmental factors such as low ionic strength, during the cell disruption process. It is also worth emphasizing the strict use of broad spectrum protease inhibitors during the cell lysis. During the affinity chromatography step, high salt concentration was necessary to avoid unspecific protein binding. The collected fractions of high β -N-acetylglucosaminidase activity were immediately ultra-filtrated to change the elution buffer into the 'long storage buffer' containing all the evaluated stabilizing supplementations including glycerol and kept at $-20\text{ }^{\circ}\text{C}$. The concentration of the enzyme samples was not larger than 2 mg/ml. The single chromatographic purification step resulted in higher than 90% homogenous, full-length and active hOGA sample (Fig. S8). Following the quality of the enzyme samples during the long time storage, their enzyme activity and homogeneity were maintained even after 12 months (Fig. S8).

2.4. Inhibitory potency of 2-acetamido-2-deoxy-D-glucono-1,5-lactone semicarbazone derivatives on hOGA and HexA/HexB activities

Michaelis-Menten kinetic parameters for *p*-nitrophenyl-GlcNAc (pNP-GlcNAc) as substrate in the presence of hOGA established in potassium-phosphate buffer at pH 7.5 resulted in 20 μM for K_M and 1.6 s^{-1} for k_{cat} values (Table 2). The determined k_{cat} value correlated well with the previously published data [44]. However, the enzyme in this study displayed much higher binding affinity toward pNP-GlcNAc than was previously reported for different conditions (Table 2). Kinetic analysis of hOGA and HexA/HexB inhibition by 2-acetamido-2-deoxy-D-glucono-1,5-lactone semicarbazone derivatives was performed by using Dixon method [45] and an improved method presented by Cornish-Bowden [46] (Fig. 3). Plotting the reciprocal initial rate against inhibitor concentration, the intersection point of the obtained curves at three different substrate concentrations was located in the fourth quadrant and gave the inhibitor constants (K_i) for all the investigated compounds (Table 3). The location of the intersection point also refers to the mode of inhibition, either competitive or mixed. Since Dixon plot cannot distinguish unambiguously between these inhibitory modes, we also plotted the kinetic data using the Cornish-Bowden method (Fig. 3). The resulting lines are parallel in the plot of $[S]/v$ against inhibitor concentration indicating competitive inhibition of hOGA and HexA/HexB enzymes by each of the 2-acetamido-2-deoxy-D-glucono-1,5-lactone semicarbazone derivatives 6.

Inhibitor constants (K_i) for most of the compounds 6 against hOGA are in the submicromolar, in some cases in the nanomolar range, and slightly higher K_i values have been obtained for HexA/

HexB (Table 3). The most potent inhibitors of hOGA are semicarbazones 6e and 6g, while thiosemicarbazone 6h proved to be the weakest one.

For the determination of the inhibitor constants of the most potent inhibitors (6e and 6g), the Dixon method could not be used in the presence of the pNP-GlcNAc substrate because the inhibitor concentration was comparable to the enzyme concentration. Therefore, the fluorogenic 4-methylumbelliferyl-GlcNAc (4-MU-GlcNAc) substrate was used to enable the application of the more sensitive fluorometric detection method. This allowed a significant decrease in the applied enzyme concentration for the inhibition studies. In a separate experiment with 6f we demonstrated that substituting the chromogenic substrate (pNP-GlcNAc) with a fluorogenic one (4-MU-GlcNAc) did not influence the binding affinity. The obtained K_i values for 6f in the presence of pNP-GlcNAc and 4-MU-GlcNAc were $0.506 \pm 0.020\text{ }\mu\text{M}$ and $0.509 \pm 0.036\text{ }\mu\text{M}$, respectively (Fig. S9).

The selectivity of inhibition of the two enzymes was moderate, and this feature resembles PUGNAc. It is worth noting the considerable difference in the inhibition by naphthyl derivatives 6f and 6g, of which the 2-naphthyl 6g is more than one order of magnitude more potent than the 1-naphthyl 6f counterpart. On the other hand, 6f is more selective towards HexA/HexB.

2.5. In silico predictions analysis

In order to gain an understanding of the factors governing the observed potencies for hOGA inhibition, computations were performed in the form of Prime protein-ligand refinements [48], followed by higher level QM/MM optimizations and QM/MM-PBSA binding free energy calculations (ΔG_{bind} , Eq. (1)).

$$\Delta G_{bind} = \Delta E_{QM/MM} + \Delta G_{solv} - T\Delta S_{MM} \quad [1]$$

Eq. (1) includes contributions from gas-phase protein-ligand interaction energies ($\Delta E_{QM/MM}$), changes in solvation free energy on binding (ΔG_{solv}), as well as the ligand entropy changes ($T\Delta S_{MM}$). In these calculations, side chains Tyr219, Phe223, Val254, Val255 and Tyr286 in the vicinity of 6a-g ligand phenyl or naphthyl rings were included as part of the QM region, selected due to the importance of these protein-ligand interactions to the observed potency differences, and to better describe π - π interactions with Tyr286. Because of the potential for a better description of binding site interactions using QM methods, QM/MM-PB(GB)SA approaches have recently been applied in a number of studies [49], including where protein-ligand π - π stacking interactions play a key role [50,51]. Here, the QM region was modelled using DFT at the M06-2X/6-31+G** level of theory, with the M06-2X functional recognised for its description of non-covalent interactions [52–54]. We should note that native ligand docking calculations with Glide [48] failed to reproduce the PUGNAc ligand crystallographic conformation (PDB code: 5UHO); more specifically the critical orientation of the phenylurethane (-O-CO-NH-Ph) moiety, so that the Prime refinement, QM/MM optimization and QM/MM-PBSA approach as fully outlined in the experimental details was applied.

The results of the QM-MM/PBSA calculations for PUGNAc and

Table 2
Michaelis-Menten kinetic parameters of hOGA for pNP-GlcNAc.

Buffer	50 mM $\text{K}_2\text{HPO}_4 - \text{KH}_2\text{PO}_4$ buffer, pH 7.5	PBS (10 mM phosphate buffer, 137 mM NaCl, 2.7 mM KCl) pH 7.4 [44]	0.5 M citrate/phosphate buffer, pH 6.5 [47]
K_M (μM)	20 ± 2	170 ± 10	1100 ± 100
k_{cat} (s^{-1})	1.6 ± 0.1	1.8 ± 0.1	3.4 ± 0.3

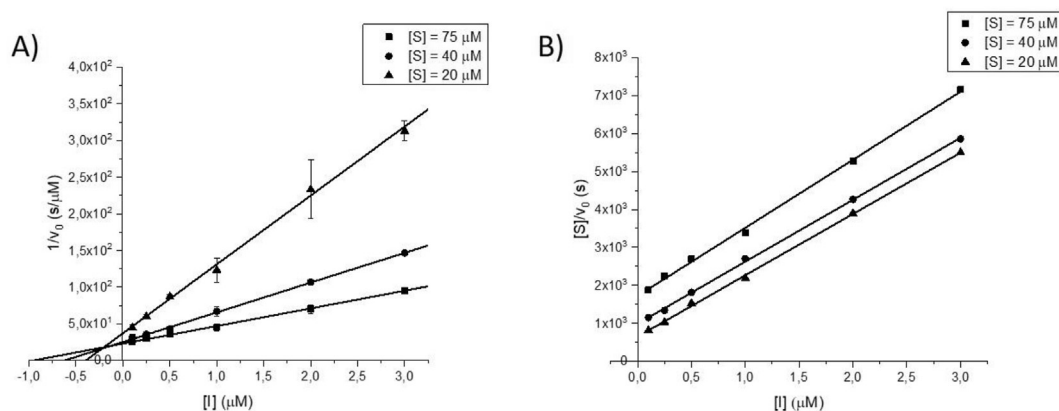
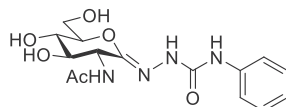
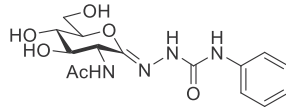
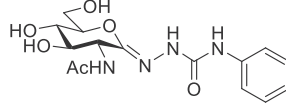
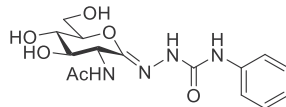
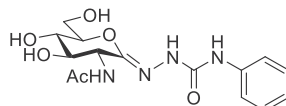
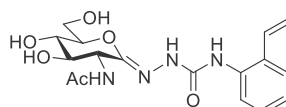
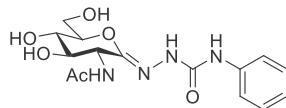
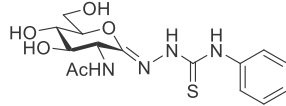


Fig. 3. Plotting hOGA inhibition data in the presence of **6a** at three different pNP-GlcNAc concentrations (■ 75 μM ; ● 40 μM ; ▲ 20 μM) by using Dixon method (A) and Cornish-Bowden method (B).

Table 3

The binding affinities of 2-acetamido-2-deoxy-D-glucono-1,5-lactone semicarbazone derivatives toward hOGA and HexA/HexB enzymes (K_i [μM]).

Compound	hOGA	HexA/HexB
6a 	0.190 ± 0.008	0.205 ± 0.014 (lit.: 0.130 ± 0.020) [29]
6b 	0.155 ± 0.003	0.332 ± 0.017
6c 	0.167 ± 0.006	0.125 ± 0.004
6d 	0.270 ± 0.010	0.413 ± 0.014
6e 	0.083 ± 0.004^a	0.170 ± 0.004
6f 	0.506 ± 0.020	0.154 ± 0.006
6g 	0.036 ± 0.001^a	0.047 ± 0.002
6h 	27 ± 3	30 ± 2

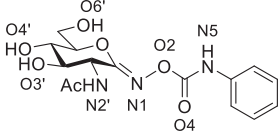
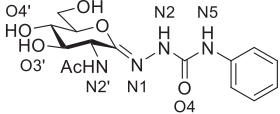
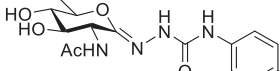
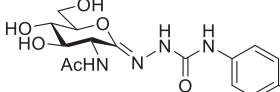
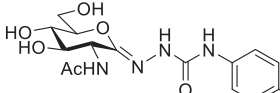
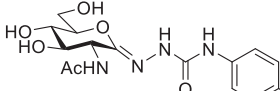
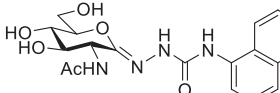
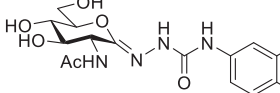
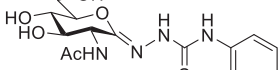
^a 4-MU-GlcNAc was used as substrate.

the eight inhibitors **6a-h** studied in this work are shown in Table 4. The final predicted ΔG_{bind} values for each inhibitor are broken down into the different contributions from $\Delta E_{QM/MM}$, ΔG_{solv} , and $T\Delta S_{MM}$. In

terms of reproducing the relative potencies, good agreement with experiment was obtained (the absolute values of predicted ΔG_{bind} are larger than experiment, an expected consequence of the

Table 4

Quantum Mechanics/Molecular Mechanics – Poisson–Boltzmann Surface Area (QM/MM-PBSA) results for the estimation of hOGA – ligand binding free energies using Eq. (1). The QM region was modelled at the M06-2X/6-31+G** level of theory; MM region using the OPLS-AA (2005) forcefield. All energy values are in kcal/mol.

Ligand	Predicted				Experimental	
	$\Delta E_{QM/MM}$	ΔG_{solv}	$T\Delta S_{MM}^a$	ΔG_{bind}	ΔG_{bind}	
PUGNAc		-136.2	96.2	-21.1	-18.9	-10.4
6a		-140.7	101.9	-21.8	-17.0	-9.5
6b		-143.1	103.3	-23.0	-16.8	-9.7
6c		-152.7	111.8	-23.3	-17.6	-9.6
6d		-147.7	109.2	-22.9	-15.6	-9.3
6e		-148.4	107.8	-22.2	-18.4	-10.0
6f		-152.2	105.8	-23.0	-23.4	-8.9
6g		-153.8	106.8	-22.7	-24.3	-10.6
6h		-145.9	119.0	-19.8	-7.1	-6.5

^a Values calculated at 310 K to be consistent with the performed kinetic experiments. Experimental $\Delta G_{bind} = RT \ln K_i$.

method approximations [50,51,55]). PUGNAc was correctly predicted as more potent than the phenylsemicarbazone analogues **6a–e**. PUGNAc and **6a** differ structurally only in terms of their -O-C(O)-NH- and -NH-C(O)-NH- moieties, respectively. Compared to PUGNAc, **6a** (and the other semicarbazone analogues, c.f. **6e** complex in Fig. 4 (A)) is able to exploit a hydrogen bond interaction from N2H (c.f. numbering scheme in Table 4) with the Tyr219 side chain hydroxyl O atom. While protein-ligand interactions based on $\Delta E_{QM/MM}$ are predicted as stronger for **6a** (-140.7 kcal/mol) compared to PUGNAc (-136.2 kcal/mol), the desolvation costs for **6a** are greater, as well as entropy costs accounted for as loss of ligand vibration, rotation and translation on binding. Thiosemicarbazone **6h** (a C=O to C=S replacement in the linker) was correctly predicted as the least potent ligand. Although its protein-

ligand ($\Delta E_{QM/MM}$) interactions are predicted as strong (-145.9 kcal/mol), the desolvation cost of binding (119.0 kcal/mol) was the highest of all inhibitors in Table 4.

Analyzing the ΔG_{bind} values for all the phenyl analogues **6a–e**, compounds **6d** and **6e** are correctly predicted as the least and most potent inhibitors within this series, respectively; the remaining inhibitors in this series (**6a–c**) displayed similar experimental potencies (0.155–0.190 μ M) and had predicted potency ranks in between. Considering the electron donating or withdrawing properties of **6a–e** para-substituents, there is no obvious correlation between these properties and the observed potencies. Indeed, considering the contributions to ΔG_{bind} , the relative potencies of **6a–e** are predicted to be a sensitive balance between protein-ligand interactions ($\Delta E_{QM/MM}$) and desolvation effects; entropy to a lesser

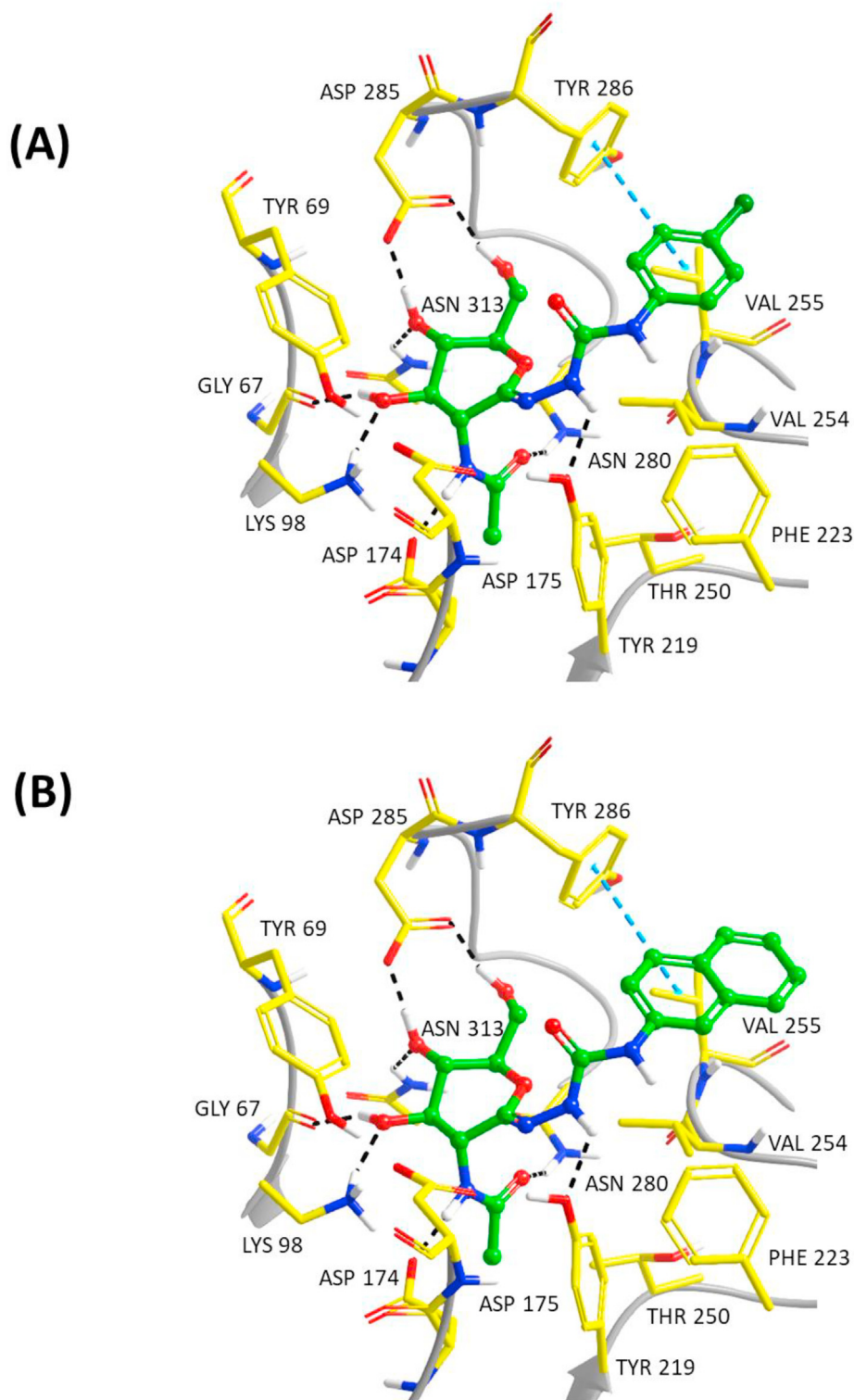


Fig. 4. Predicted model complexes from Prime, QM/MM and QM/MM-PBSA calculations: (A) hOGA-**6e** and (B) hOGA-**6g**.

degree. Given the good agreement between relative ΔG_{bind} predicted and experimental values for the phenyl substituted compound series (Spearman rank correlation $R_s = 0.893$ ($p < 0.01$); Pearson correlation $R_p = 0.993$ ($p < 0.01$) – for PUGNAc, **6a-e** and **6h**), the predicted binding interactions could be analysed with confidence.

The most potent phenyl analogue **6e** has the strongest protein-

ligand interactions ($\Delta E_{QM/MM} = -148.4$ kcal/mol), and its predicted protein-ligand complex is shown in Fig. 4 (A). The crystallographic *N*-acetyl-glucosamine moiety interactions in hOGA – PUGNAc (PDB code: 5UHO) are, as expected, conserved in the predicted complexes for the newly designed ligands **6a-h**. These include key hydrogen bond interactions of inhibitor O4' and O6' hydroxyls (c.f. Table 4) with Asp285 side chain carboxylate; O4'-hydroxyl O with

the Asn313 side chain amide; and O3'-hydroxyl with both Gly67 backbone O and Lys98 side chain. The *N*-acetyl group is involved in hydrogen bonds with Asp174 side chain carboxylate and Asn280 side chain amide. Considering the binding interactions of the phenyl substituents of **6a–6e** (and **6h**), there are favourable interactions with the hydrophobic side chains of Tyr219, Phe223, Val254, Val255 and Tyr286. Of particular significance are edge-to-face T-shaped π - π stacking with Tyr286. Although the rings are not ideally aligned, the π - π stacking ring centroid – ring centroid distances for **6a – 6e** were in the range 5.3–5.5 Å (5.4 Å for **6e** in Fig. 4 (A)), close to theoretical optimum intermonomer distances (~4.8–5.0 Å) in simple model systems [56] and within the observed geometric preferences (5.0–5.6 Å) of protein – ligand (Phe – phenyl) T-shaped π - π interactions from Protein Data Bank analysis [57]. The protein-ligand ring planes had intersection angles 83.5°–86.8°, that are also consistent with the T-stacking Protein Data Bank analysis [57]. Accounting for phenyl substituent effects for T-shaped configurations can be somewhat more complex than for sandwich arrangements [58]; in our situation (**6a–e**), the ligand π – π interactions with Tyr286, are accompanied by additional direct interactions between the ligand phenyl substituents and the phenol ring of Tyr286.

Of further significance, we observed the potential for binding site loop Val255 (backbone) NH – π interactions with the designed compounds. For the **6e** complex (Fig. 4 (A)), the Val255 NH to centroid of **6e** phenyl ring predicted distance was relatively long at 3.8 Å. This analysis, in part, was the basis of our decision to explore naphthyl substituents that could better exploit such interactions (*vide infra*). Compound **6e**, however, had the additional potential to form halogen Cl – hydrogen bond donor (HBD) interactions with Val255 NH. A quite recent QM study and survey of crystal structure data demonstrated that halogen (X) – HBD interactions can make significant contributions to ligand–protein binding [59]. Geometric parameters considered by the authors included the angle C–X–HBD and the distance HBD – X, with the HBD defined by its oxygen, nitrogen or sulfur atom. The survey revealed C–X–HBD angle maxima in the plots in the range ~80°–110°. While the predicted C–X–HBD angle (66°) and HBD – X distance (4.9 Å) for the hOGA – **6e** predicted model complex are also not optimum for halogen – HBD interactions, these interactions can occur over a broad range of angles and we must also consider that Val255 is part of a loop. Additionally, from the crystal structure data analysis, 60°–70° angles for nitrogen as HBD were associated with mainly longer 4.0–4.5 Å distances. We can therefore postulate that the Val255 NH–Cl interaction may contribute to the improved potency of **6e** compared to the other analogues **6a–6d**.

As mentioned, it was decided to explore whether substitution of the phenyls of **6a–6e** with naphthyl moieties could better exploit potential NH – π contacts with Val255, but also the hydrophobic nature of other surrounding residues. Indeed, predictions for both 1- (**6f**) and 2-naphthyl (**6g**) suggested improved potency, with predicted ΔG_{bind} values of –23.4 and –24.3 kcal/mol, respectively. And while the prediction was incorrect for **6f**, potentially due to conformational entropy effects (over-prediction of 1-naphthalene compound analogues extends to other methods and systems [60]), **6g** was experimentally the most potent of all ligands tested. The predicted binding of **6g** with a 2-naphthyl moiety did as anticipated lead to better Val255 NH – π contacts (3.4 Å to centroid of ring extension), as well as preserving the edge-to-face T-shaped contacts with Tyr286 (Fig. 4 (B)). The $\Delta E_{QM/MM}$ value of –153.9 kcal/mol was considerably more favourable (>5 kcal/mol) to those obtained for the substituted phenyls. An alternative parallel conformation π - π binding mode with Tyr286 was also predicted for **6g**, but was less favourable ($\Delta G_{bind} = -11.4$ kcal/mol) compared to the T-shaped conformation ($\Delta G_{bind} = -25.0$ kcal/mol); in agreement, T-

shaped binding conformations are reported as more predominant for solved protein–ligand complexes [57].

3. Conclusion

A series of 2-acetamido-2-deoxy-D-glucono-1,5-lactone 4-aryl(thio)semicarbazone derivatives was obtained by a five-step synthetic sequence from D-glucosamine with overall yields of 15–55%. These compounds represent the first analogues of PUGNAc with modified linkers between the sugar and the aromatic moiety. An efficient heterologous expression protocol for full length and active recombinant hOGA was developed by *E. coli* strain selection and optimization of cultivation conditions. Thermal denaturation studies revealed environmental factors that most affected hOGA stability, so that hOGA samples displayed long-term stability and ensured reproducibility in the evaluation of inhibitory potencies. Kinetic studies with hOGA and hexosaminidases A and B showed competitive inhibition for all synthesized semicarbazone derivatives (hOGA: range of K_i -s ~30–250 nM; HexA/HexB: range of K_i -s ~50–400 nM) with a modest selectivity towards hOGA. These lactone semicarbazones are therefore alternatives of the OGA inhibitor PUGNAc in terms of both synthetic efficiency and inhibitory efficacy. A computational approach consisting of Prime protein–ligand refinements, post-processed by QM/MM optimizations and calculation of binding free energies using QM/MM-PBSA proved effective, for the most part, to describe the interactions governing the observed ligand potencies. The most potent inhibitor **6g** ($K_i = 36$ nM) had a 2-naphthyl substituent that better exploited interactions (including NH – π and T-shaped π – π stacking), with surrounding hydrophobic residues. Further computational and synthetic work to enhance hOGA selectivity is in progress and will be disclosed in due course.

4. Experimental

4.1. Syntheses

4.1.1. General methods

Melting points were measured on a Kofler hot-stage and are uncorrected. Optical rotations were determined with a Perkin–Elmer 241 or Jasco P-2000 (Easton, MD, USA) polarimeters at room temperature. NMR spectra were recorded by Bruker AM Avance 360 (360/90 MHz for $^1\text{H}/^{13}\text{C}$) spectrometer. Chemical shifts are referenced to TMS as the internal reference (^1H), or to the residual solvent signals (^{13}C). 2D ^1H – ^{13}C HMBC experiment [32] optimized to long-range heteronuclear coupling of 8 Hz, and 2D ^1H – ^1H EASY ROESY experiment [33] with 300 ms mixing time were performed on a Bruker Avance II 500 MHz spectrometer equipped with a 5 mm z-gradient TXI probe. Mass spectra were recorded with MicroTOF-Q type Qq-TOF MS and maXis II UHR ESI-QTOF MS (Bruker Daltonik, Bremen, Germany) instruments in positive ion mode with electrospray ionization or atmospheric pressure chemical ionization technique. TLC plates were visualized under UV light, and by spray reagent with gentle heating (the plate was sprayed with the following solution: abs. EtOH (95 ml), cc H₂SO₄ (5 ml), anisaldehyde (1 ml)). For column chromatography Kieselgel 60 (Merck, particle size (0.063–0.200 mm) was applied. Dichloromethane was distilled from P₂O₅ and stored over 4 Å molecular sieves. Pyridine was distilled from KOH and stored over KOH. CrO₃ was stored over P₂O₅. 4-Phenylsemicarbazide (**2a**) and 4-phenylthiosemicarbazide (**2h**) were purchased from Sigma-Aldrich Ltd. (Budapest, Hungary). 2-acetamido-3,4,6-tri-*O*-acetyl-2-deoxy- α , β -D-glucopyranose (**1**) [30,31], substituted phenylsemicarbazides (**2b–e**) and 1- or 2-naphthylsemicarbazides (**2f–g**) [61] were synthesized according to literature procedures. Unless

otherwise indicated, all chemicals used in the biochemical experiments were analytical-grade and purchased from Sigma-Aldrich Ltd. (Budapest, Hungary).

4.1.2. General procedure I. for the synthesis of 1-(2-acetamido-3,4,6-tri-O-acetyl-2-deoxy- β -D-glucopyranosyl)-(thio)semicarbazides (3a-h)

A solution of 200 mg (0.58 mmol) 2-acetamido-3,4,6-tri-O-acetyl-2-deoxy- α , β -D-glucopyranose (**1**), 0.87 mmol (thio)semicarbazide and 0.058 mmol *p*-toluenesulfonic acid in 4 ml chloroform were boiled under reflux until the reactions were complete (monitored by TLC hexane: acetone = 3 : 2). The mixtures were cooled in ice-bath, the white precipitates were filtered. If the reagents contaminated the products, column chromatography was used (hexane: acetone 1 : 1).

4.1.3. General procedure II. for the synthesis of 2-acetamido-3,4,6-tri-O-acetyl-2-deoxy-D-glucono-1,5-lactone semicarbazones (5a-h)

Method A: A solution of 4 equivalents of anhyd. pyridine in 2 ml of anhyd. CH_2Cl_2 was stirred at 25 °C as 2 equivalents of dry CrO_3 were added in one portion. The reaction was slightly exothermic, and the solution turned burgundy. After 20 min at 25 °C, the solution was cooled to 0 °C and a suspension of 100 mg compound in 3 ml of anhyd. CH_2Cl_2 was added in one portion. The reaction mixture was stirred, while it slowly warmed up to room temperature. After the reaction was complete (monitored by TLC hexane: acetone 1 : 1) it was diluted with 4 ml of Et_2O . The mixture was filtered under vacuum and the filtrate concentrated. The pyridine was removed under high vacuum, and the residue was purified by column chromatography (hexane: acetone 2:1).

Method B: Activated MnO_2 was added to a solution of 100 mg compound in anhyd. CH_2Cl_2 . The mixture was boiled until the reaction was complete (hexane: acetone 1:1), the MnO_2 was filtered under vacuum and the filtrate concentrated, the residue was purified by column chromatography (hexane: acetone 2:1).

4.1.4. General procedure III. for the synthesis of 2-acetamido-2-deoxy-D-glucono-1,5-lactone semicarbazones (6a-h)

A solution of 100 mg compound in 1 ml of MeOH was stirred at 25 °C with 1 ml of a sat. NH_3/MeOH solution. After the reaction was complete (monitored by TLC, CHCl_3 : MeOH 7:3) the solvent was removed and the residue was purified by column chromatography or was recrystallized (MeOH).

4.1.5. Synthesis and characterization of the new compounds

Detailed synthetic procedures and compound characterization data can be found in the electronic supplementary information.

4.2. Biochemical materials and methods

4.2.1. Microorganisms and culture conditions

Five different *Escherichia coli* strains were used for the expression of the long isomorph of hOGA: *E. coli* BL21(DE3), *E. coli* BL21(DE3) pLysS (from Novagen), *E. coli* BL21- CodonPlus (DE3)-RIPL (from Stratagene) and *E. coli* BL21 STAR(DE3) (from Invitrogen) and *E. coli* BL21(DE3) Rosetta. hOGA encoding gene was inserted between NdeI and XhoI restriction site of pET28b plasmid carrying kanamycin resistance. The resulting vector construction was kindly provided by prof. D. J. Voadlo from Simon Fraser University (Burnaby, Canada) [62]. The vector construct carrying hOGA encoding gene was transformed into the five *E. coli* strains by the heat-shock methods [63]. Resulting transformant cells of the different strains, were subjected to the protein expression procedure.

4.2.2. Heterologous expression of human OGA in *E. coli*

4.2.2.1. Small scale protein expression. Small scale expressions were performed in 250 ml Luria broth (LB) growth medium supplemented with 50 $\mu\text{g}/\text{ml}$ kanamycin antibiotics in 1L Erlenmeyer flasks and inoculated with 1 ml starter cultures of the different *E. coli* strains. They were grown overnight from a single colony, at 37 °C. The growing temperature of the small-scale expression was varied between 16 and 37 °C, specifically 16 °C, 23 °C and 28 °C. OGA enzyme was expressed by induction with 0.4 mM IPTG at about mid-log phase, OD_{600} ~0.6 or 0.9. Bacterial cells were harvested at stationary phase (OD_{600} ~ 1.4) by centrifugation at 6000 rpm for 20 min at 4 °C. The isolated pellet (~1.2–1.6 g) was kept at –20 °C for the later isolation procedures. The frozen pellet was re-suspended in 30 ml of lysis buffer (50 mM potassium-phosphate buffer, pH 7.5, containing 1 mM DTT, 0.5% Tween 20, Protease inhibitor cocktail (P8849, Sigma Aldrich, Hungary) and 0.1 mg/ml lysozyme) and kept on ice for 30 min. In addition to lysozyme, lysis was also performed by using an Ultrasonic Homogenizer UW 2070 (from Bandelin Electronic), at 4 °C. The resulting lysates were incubated with DNase in the presence of 1 mM MgCl_2 , for 120 min, at 10 °C. Soluble fraction of the lysate was separated by centrifugation at 15,000 rpm, at 4 °C and was kept at 4 °C for the chromatographic separation which followed. During the expression and lysis, samples were collected for further characterization by gel electrophoresis, hexosaminidase activity testing and protein content determination, by the Bradford method, using BSA for the calibration curve [64].

4.2.2.2. Large-scale protein expression. Starter culture of *E. coli* Rosetta (DE3) strain was prepared (7 × 2 ml) to inoculate 500 ml kanamycine (50 $\mu\text{g}/\text{ml}$) supplemented LB medium in Erlenmeyer flasks (7 × 500 ml). The cells were grown at 23 °C, until OD_{600} reached mid-log phase (~0.9), whereupon by adding 0.4 mM IPTG the induction was carried out. The incubation of the growth was continued until the stationary phase, when cells were harvested by centrifugation at 5000 rpm for 20 min at 4 °C. The collected pellet was weighed (~27 g) and kept frozen at –20 °C. Lysis was carried out using the frozen sample by following the same procedure mentioned above (“small scale protein expression” section) except less lysis buffer was used to suspend the pellet in relation to “pellet mass/lysis volume” ratio (27 g pellet was dissolved in 400 ml lysis buffer).

4.2.3. Chromatography of hOGA

The long isomorph of hOGA protein was expressed as a fusion protein with an N-terminal His-tag comprising of hexapeptide of histidine. HiPrep IMAC Fast Flow (diameter 16 mm, length 10 mm; GE-Healthcare) column was charged up with Co^{2+} and pre-equilibrated with 20 mM potassium-phosphate buffer, pH = 7.7, containing 0.5 M KCl, 50 mM imidazole and 0.5% Tween 20 as binding buffer. The bound hOGA protein was eluted with a 50–500 mM linear imidazole gradient in 20 mM potassium-phosphate buffer, pH = 7.7, containing 0.5 M KCl over 20 column volumes. The N-acetylglucosaminidase activity and the protein content of the fractions were determined. Those with the highest N-acetylglucosaminidase activity were pooled together and ultrafiltrated (Amicon Ultra – 100 kDa, Merck Millipore) for a buffer exchange, into 50 mM potassium-phosphate buffer, pH = 7.5 containing 1 mM PMSF, 1 mM DTT, 1 mM EDTA and 30% glycerol. The enzyme sample was stored at –20 °C in small aliquots.

4.2.4. N-acetylglucosaminidase activity assay

The N-acetylglucosaminidase activity of hOGA enzyme was determined using pNP-GlcNAc substrate. Upon enzyme action, p-nitrophenol is liberated from the substrate in the enzyme-substrate

reaction mixture. Quenching the enzyme effect by adding strong alkaline solution to the reaction mixture, the liberated *p*-nitrophenol product was detected by measuring the absorbance at 400 nm. For quantitative product estimation, the *p*-nitrophenol calibration curve was determined in a solution that contains one volume of the assay buffer and two volumes of the 0.2 M Na₂HPO₄/NaOH solution, pH = 12.0. *N*-acetylglucosaminidase activity determination was performed in 200 μl of 50 mM potassium phosphate buffer, pH = 7.5, containing 0.2 mM *p*NP-GlcNAc as a substrate, which was pre-incubated in 37 °C. The enzyme reaction was started by adding a 50 μl hOGA sample to the above solution, incubating the reaction mixture at 37 °C, for 5 min. This reaction was then stopped by adding 500 μl of 0.2 M Na₂HPO₄/NaOH solution, pH = 12.0. The absorbance at 400 nm of the quenched reaction was followed and the enzyme activity was calculated in units of μmol/min.

4.2.5. Stability studies on hOGA

Thermal stability of hOGA was measured by incubating the enzyme at 50 °C in different solutions of varying the present cation and its concentration, the type of reducing agents, the type of detergents and their concentrations. In all cases, the stability studies were carried out by incubating 0.33 mg/ml hOGA at 50 °C, and, at regular intervals (5 min for the first half hour, then every 10 min) samples (10 μl) were taken and were placed on ice. For the incubation of hOGA samples, Thermalmixer MKR 13 (by HLC BioTech) was used by applying 200 rpm shaking. To the incubated samples, placed on ice, 40 μl distilled water was added then the *N*-acetylglucosaminidase activity was measured by following the protocol described above. The sodium and potassium ion influence on the enzyme thermal stability was tested in 50 mM phosphate buffer, pH 7.5, containing 0.3 M KCl and 0.3 M NaCl. Thermal stability of hOGA in the presence of different reducing agents such as DTT (1 mM) and β-mercaptoethanol (1 mM) was also determined in 50 mM phosphate buffer, pH 7.5 as well as the effect of different detergents including 0.5% Tween 20, 0.5% Triton X-100 and glycerol in the same buffer. In all measurements the ratios of the *N*-acetylglucosaminidase activity determined at a given time interval (A_t) and at zero time (A_0) were calculated as residual activities (A_t/A_0). Residual activity was then plotted against time. The data points were fitted to a single step transition, from the native enzyme conformation to the denatured enzyme form ($E_N \rightarrow E_D$), that followed first order kinetics: $d[E_N]/t = -k_D[E_N]$, where k_D is the thermal denaturation rate (min^{-1}). The active enzyme concentration ($[E_N]$) is expressed as the residual enzyme activity (A_t/A_0). Fitting residual activity vs incubation time according to the single exponential decay curve, $\ln A_t/A_0$ will be constant and gives k_D . For data fitting and graphic representation Origin-Pro-8 (OriginLab Corp. Northampton, MA, USA) was used.

Data points for residual activity versus time, giving sigmoidal curve, were modelled by using logistic equation (Eq. (2)):

$$y = A1 + \frac{A2 - A1}{1 + 10^{(\log x_0 - x)p}} \quad [2]$$

where $A1$ is the bottom asymptote, $A2$ top asymptote, $\log x_0$ center, p : slope factor that decides the steepness of the curve [65]. The logistic function is used for describing the rate of autocatalytic processes [66]. In this case y is residual activity, x is time, $\log x_0$ the time needed for the denaturation of the half protein population (half-life).

Residual activity versus time, which resulted in a biphasic sigmoid curve, can be fitted by biphasic logistic equation (Eq. (3)):

$$y = A1 + (A2 - A1) \left[\frac{p}{1 + 10^{(\log x_{01} - x)h1}} + \frac{1 - p}{1 + 10^{(\log x_{02} - x)h2}} \right] \quad [3]$$

where $A1$ is the bottom asymptote, $A2$ top asymptote, $\log x_{01}$ centre of the first phase, $\log x_{02}$ centre of the second phase, $h1$ slope of the first phase, $h2$ slope of the second phase, p proportion between the phases. In this case, two-state transition was observed during the denaturation of the protein, the inflexion points ($\log x_{01}$, $\log x_{02}$) of the biphasic sigmoid curve gives the time ($t_{1/2}$) needed to reach half-maximal of each phase.

4.2.6. Kinetic studies

For determining the Michaelis-Menten constants of OGA for *p*NP-GlcNAc and 4-MU-GlcNAc substrates, the enzymatic reactions were performed in 50 mM potassium phosphate buffer (pH 7.5) in a final volume of 1 ml, at 37 °C, containing varied final substrate concentrations. These ranged from 2 mM to 5 μM (for both substrates) in the presence of two hOGA concentrations, namely 33 nM and 82 nM in case of *p*NP-GlcNAc and 3 nM in case of 4-MU-GlcNAc. Using *p*NP-GlcNAc substrate the reaction was conducted in 1 ml cuvettes held in the thermostated cell holder of AnalytikJena Specord 250 plus double beam spectrophotometer. On addition of the enzyme, the reactions were monitored continuously at 400 nm. Using fluorogenic 4-MU-GlcNAc substrate, the reactions were set up in a fluorescence cuvette, held in thermostated cell holder of Jasco FP-8200 fluorescence spectrophotometer equipped with a Xe lamp light source at 37 °C. The reactions were initiated by the addition of 4-MU-GlcNAc and the liberated fluorescent product, 4-methylumbelliferone, was followed with excitation at 360 nm, and emission was detected at 450 nm every 10 s for 10 min. For determining the Michaelis-Menten constants of HexA/HexB for *p*NP-GlcNAc substrate, the enzymatic reactions were performed in 50 mM potassium phosphate buffer (pH 5.8) in a final volume of 1 ml, at 37 °C. The substrate concentrations used ranged from 5 mM to 60 μM in the presence of 5.0 mU of HexA/HexB (from bovine kidney, Sigma Aldrich). Initial velocities were calculated within the linear region of the reaction progress curves obtained from using both the chromogenic and fluorogenic substrates, then Michaelis–Menten kinetic parameters were calculated through nonlinear regression of Michaelian saturation curves using Origin-Pro-8 (OriginLab Corp. Northampton, MA, USA). Initial velocities were expressed in μM of liberated product in 1 s as it was determined from the calibration curves of the liberated *p*NP. All the measurements were performed in triplicates.

4.2.7. Inhibition studies

All target compounds were evaluated for their inhibitory activities against hOGA and HexA/HexB. Inhibition studies were performed at three substrate concentrations (20 μM, 40 μM and 75 μM for *p*NP-GlcNAc and 7.5 μM, 12.5 μM and 25 μM for 4-MU-GlcNAc) in a reaction mixture containing 50 mM potassium phosphate buffer (pH 7.5), final concentration of synthesized inhibitors (**6a-g**) ranging from 0 to 3 μM or from 0 to 200 μM for **6h**, in the presence of 33 nM hOGA. In experiments using fluorogenic substrate, 3 nM hOGA was applied in the presence of **6e** and **6g** inhibitors, their concentrations ranged from 0 nM to 100 nM. In case of HexA/HexB the *p*NP-GlcNAc concentrations were 0.5 mM, 1.0 mM and 1.5 mM, except for **6e** and **6h**, where concentrations were 0.8 mM, 1.0 mM and 1.5 mM. The concentration of the inhibitors was in the 0–1 μM range, except for **6h** where the range was from 0 to 50 μM.

In all cases the enzyme and the inhibitors were pre-incubated at 37 °C. The reactions were initiated by the addition of the substrate solution and the kinetic curves were recorded as described above.

Initial velocities were estimated and the reciprocal of initial velocities plotted against inhibitor concentrations. All measurements were performed in triplicates. Inhibition constants (K_i) were determined by linear regression of data from Dixon plots [45]. The modality of the inhibition were assessed for the investigated compounds according to the Cornish-Bowden method [46].

4.3. Computational details

4.3.1. Protein preparation

hOGA was prepared for the initial Prime refinement calculations using Schrödinger's Protein Preparation Wizard [48] and the solved 3.21 Å resolution co-crystallized complex of the protein (chains A-D) with PUGNac (PDB code 5UHO). The waters within 5 Å of PUGNac were initially retained (deleted for subsequent calculations), bond orders assigned and hydrogens added, with protonation states for basic and acidic residues based on calculated pK_a 's at pH 7 from PROPKA [67]. Subsequent optimization of hydroxyls, histidine protonation states and C/N atom flips, as well as side chain O/N atom flips of Gln and Asn residues was based on optimizing hydrogen bonding patterns. The system was then minimized using OPLS-AA (2005) forcefield [68] with the RMSD (heavy atoms) maintained to within 0.3 Å of the crystallographic positions.

4.3.2. Prime protein-ligand complex refinements

Initial models of protein-ligand complexes for each of the inhibitors **6a-h** were prepared by mutation of the relevant atoms in the PUGNac ligand in chain A of the prepared crystallographic hOGA-PUGNac complex (PDB code: 5UHO; section 4.1.1). For the naphthyl analogues, rings were extended by fusing at both ortho-meta positions for 1-naphthalene and both meta-para positions for 2-naphthalene. Prime v5.4 protein-ligand refinements [48] were then performed in local optimization mode for each new complex. Default settings were employed that included the OPLSe forcefield [69] and VSGB model of solvation [70]. Residues within 5 Å of PUGNac in 5UHO were selected to be free in all refinements (same 360 atoms), with the rest of the protein atoms constrained. The method was also applied to the native PUGNac ligand; comparing the Prime refined protein-ligand model with the crystal structure complex (following backbone superimposition), small RMSDs (heavy atoms) of 0.821 Å and 0.430 Å were obtained for ligand and flexible binding site residues, respectively.

4.3.3. QM/MM and QM/MM-PBSA calculations

The Prime refined protein-ligand complexes for each ligand were used as input for QM/MM gas phase optimizations. In these calculations, the same protein residues were free and constrained as per the Prime refinements described above. The QM region consisted of the respective ligand and side chains of key binding site residues (Try219, Phe223, Val254, Val255 and Tyr286 of chain A) surrounding the phenyl/naphthyl ligand substituents, and was modelled using DFT with the M06-2X functional [53] and the 6-31+G** basis set [71,72]; the rest of the systems were modelled using MM with the OPLS-AA(2005) forcefield [68]. For the QM with MM interface, hydrogen caps on the QM region residue side chains were used. No cut-off was used for non-bonded interactions. The MM region effectively polarizes the QM region, with interactions between QM and MM regions including electrostatic effects between the MM point charges and the QM wavefunction, as well as van der Waals terms between QM and MM atoms [73]. The optimized complexes were then used as input for single-point QM/MM-PBSA calculations [55], where the binding free energies (ΔG_{bind}) were calculated as the difference in energies between the bound and the unbound states of the protein-ligand complexes using Eq. Eq. (1).

In Eq. (1), $E_{QM/MM}$ is the gas phase QM/MM energy; and G_{solv} , the solvation free energy. For the latter, bulk solvation (water) effects were included using Poisson-Boltzmann Surface Area (PBSA) approach [74], with the default solute (internal) dielectric constant of 1.0 used. Otherwise, the QM and MM regions were modelled the same as for the preceding QM/MM optimizations. The final term in Eq. (1) includes a MM estimate (OPLS-AA(2005) forcefield [68]) for the loss of ligand entropy (ΔS_{MM}) on binding calculated using the Rigid Rotor Harmonic Oscillator (RRHO) approximation, which considers the vibrational, rotational and translational (VRT) entropy of the ligands; RRHO calculations were run using MacroModel v12.2 [48]. All QM/MM and QM/MM-PBSA calculations were performed using QSite (Jaguar v10.2; Impact v81012) [48]. Corrections for basis set superimposition error (BSSE) as a result of incomplete basis sets are not included with the Schrödinger qsite_binding_energies.py script used for QM/MM-PBSA calculations. However, it was important to probe the potential effects of neglect of BSSE on the predicted relative potencies (reported ΔG_{bind} values). Accordingly, Jaguar v10.2 [48] gas phase QM calculations (M06-2X/6-31+G**) on simplified model complexes of the inhibitors were performed using an approach previously described [50]. In these calculations the complexes consisted only of hydrogen capped side chains of residues from the QM region (Try219, Phe223, Val254, Val255 and Tyr286) and the ligands. Estimated BSSE effects calculated using the Boys-Bernardi counterpoise (CP) method [75] revealed values ranging 2.5–3.0 kcal/mol and $\Delta E_{QM/MM}$ values were corrected accordingly using the following equation [50]:

$$\Delta E_{QM/MM} = \Delta E_{QM/MM}^{uncorr} + BSSE. \quad [4]$$

Declaration of competing interest

The authors declare that they have no known competing financial interests or personal relationships that could have appeared to influence the work reported in this paper.

Acknowledgement

This work was financially supported by the National Research, Development and Innovation Office of Hungary (Grants: 109450, FK-125067 and PD 135034) and by the EU and co-financed by the European Regional Development Fund under the projects GINOP-2.3.2-15-2016-00008 and GINOP-2.3.3-15-2016-00004. I.T. acknowledges the support of the János Bolyai Research Scholarship of the Hungarian Academy of Sciences (BO/00372/20/7) and the ÚNKP-20-5-DE-262 New National Excellence Program of the Ministry for Innovation and Technology from the source of the National Research, Development and Innovation Fund.

Appendix A. Supplementary data

Supplementary data to this article can be found online at <https://doi.org/10.1016/j.ejmech.2021.113649>.

References

- [1] X. Yang, K. Qian, Protein O-GlcNAcylation: emerging mechanisms and functions, *Nat. Rev. Mol. Cell Biol.* 18 (2017) 452–465.
- [2] J. Ma, C. Wu, G.W. Hart, Analytical and biochemical perspectives of protein O-GlcNAcylation, *Chem. Rev.* 121 (2021) 1513–1581.
- [3] M.S. Macauley, D.J. Vocadlo, Enzymatic characterization and inhibition of the nuclear variant of human O-GlcNAcase, *Carbohydr. Res.* 344 (2009) 1079–1084.
- [4] G.W. Hart, Nutrient regulation of signaling and transcription, *J. Biol. Chem.* 294 (2019) 2211–2231.

- [5] D. Wu, Y. Cai, J. Jin, Potential coordination role between O-GlcNAcylation and epigenetics, *Protein & Cell* 8 (2017) 713–723.
- [6] C. Liu, J. Li, O-GlcNAc: a sweetheart of the cell cycle and DNA damage response, *Front. Endocrinol.* 9 (2018).
- [7] Y.R. Yang, M. Song, H. Lee, Y. Jeon, E.-J. Choi, H.-J. Jang, H.Y. Moon, H.-Y. Byun, E.-K. Kim, D.H. Kim, M.N. Lee, A. Koh, J. Ghim, J.H. Choi, W. Lee-Kwon, K.T. Kim, S.H. Ryu, P.-G. Suh, O-GlcNAc is essential for embryonic development and maintenance of genomic stability, *Aging Cell* 11 (2012) 439–448.
- [8] C. Guinez, A.-M. Mir, V. Dehennaut, R. Cacan, A. Harduin-Lepers, J.-C. Michalski, T. Lefebvre, Protein ubiquitination is modulated by O-GlcNAc glycosylation, *Faseb. J.* 22 (2008) 2901–2911.
- [9] C.M. Ferrer, V.L. Sodi, M.J. Reginato, O-GlcNAcylation in cancer biology: linking metabolism and signaling, *J. Mol. Biol.* 428 (2016) 3282–3294.
- [10] W.Y. Wani, J.C. Chatham, V. Darley-Usmar, L.L. McMahon, J. Zhang, O-GlcNAcylation and neurodegeneration, *Brain Res. Bull.* 133 (2017) 80–87.
- [11] C.-X. Gong, F. Liu, K. Iqbal, O-GlcNAcylation: a regulator of tau pathology and neurodegeneration, *Alzheimer's Dementia* 12 (2016) 1078–1089.
- [12] A.F. Abdel-Magid, Inhibition of O-GlcNAcase (OGA): a potential therapeutic target to treat Alzheimer's disease, *ACS Med. Chem. Lett.* 5 (2014) 1270–1271.
- [13] X.H. Wang, W.P. Li, J. Marcus, M. Pearson, L.X. Song, K. Smith, G. Terracina, J.L. Lee, K.L.K. Hong, S.X. Lu, L. Hyde, S.C. Chen, D. Kinsley, J.P. Melchor, D.J. Rubins, X.J. Meng, E. Hostetler, C. Sur, L.L. Zhang, J.B. Schachter, J.F. Hess, H.G. Selnick, D.J. Vocadlo, E.J. McEachern, J.M. Uslander, J.L. Duffy, S.M. Smith, MK-8719, a novel and selective O-GlcNAcase inhibitor that reduces the formation of pathological tau and ameliorates neurodegeneration in a mouse model of tauopathy, *J. Pharmacol. Exp. Therapeut.* 374 (2020) 252–263.
- [14] B.L. Cantarel, P.M. Coutinho, C. Rancurel, T. Bernard, V. Lombard, B. Henrissat, The Carbohydrate-Active Enzymes database (CAZY): an expert resource for Glycogenomics, *Nucleic Acids Res.* 37 (2009) D233–D238.
- [15] Y. He, M.S. Macauley, K.A. Stubbs, D.J. Vocadlo, G.J. Davies, Visualizing the reaction coordinate of an O-GlcNAc hydrolase, *J. Am. Chem. Soc.* 132 (2010) 1807–1809.
- [16] M.J. Lemieux, B.L. Mark, M.M. Cherney, S.G. Withers, D.J. Mahuran, M.N.G. James, Crystallographic structure of human β -hexosaminidase A: interpretation of Tay-Sachs mutations and loss of GM2 ganglioside hydrolysis, *J. Mol. Biol.* 359 (2006) 913–929.
- [17] N. Çetinbaş, M.S. Macauley, K.A. Stubbs, R. Drapala, D.J. Vocadlo, Identification of Asp174 and Asp175 as the key catalytic residues of human O-GlcNAcase by functional analysis of site-directed mutants, *Biochemistry* 45 (2006) 3835–3844.
- [18] B.L. Mark, D.J. Vocadlo, S. Knapp, B.L. Triggs-Raine, S.G. Withers, M.N.G. James, Crystallographic evidence for substrate-assisted catalysis in a bacterial β -hexosaminidase, *J. Biol. Chem.* 276 (2001) 10330–10337.
- [19] S.K. Srivastava, E. Beutler, Hexosaminidase-A and hexosaminidase-B: studies in Tay-Sachs' and Sandhoff's disease, *Nature* 241 (1973), 463–463.
- [20] S.T. Hepbildikler, R. Sandhoff, M. Kölzer, R.L. Proia, K. Sandhoff, Physiological substrates for human lysosomal β -hexosaminidase S, *J. Biol. Chem.* 277 (2002) 2562–2572.
- [21] J. Popko, J. Marciniak, A. Zalewska, P. Małdyk, M. Rogalski, K. Zwierz, The activity of exoglycosidases in the synovial membrane and knee fluid of patients with rheumatoid arthritis and juvenile idiopathic arthritis, *Scand. J. Rheumatol.* 35 (2006) 189–192.
- [22] J. Popko, A. Zalewska, S. Olszewski, A. Górka, S. Serakowski, K. Zwierz, M. Urban, Activity of N-acetyl- β -hexosaminidase in serum and joint fluid of the knees of patients with juvenile idiopathic arthritis, *Clin. Exp. Rheumatol.* 21 (2003) 675.
- [23] D.L. Dong, G.W. Hart, Purification and characterization of an O-GlcNAc selective N-acetyl- β -D-glucosaminidase from rat spleen cytosol, *J. Biol. Chem.* 269 (1994) 19321–19330.
- [24] M.S. Macauley, A.K. Bubb, C. Martinez-Fleites, G.J. Davies, D.J. Vocadlo, Elevation of global O-GlcNAc levels in 3T3-L1 adipocytes by selective inhibition of O-GlcNAcase does not induce insulin resistance, *J. Biol. Chem.* 283 (2008) 34687–34695.
- [25] A.A. Elbatrawy, E.J. Kim, G. Nam, O-GlcNAcase: emerging mechanism, substrate recognition and small-molecule inhibitors, *ChemMedChem* 15 (2020) 1244–1257.
- [26] M. Hattie, N. Cekić, A.W. Debowski, D.J. Vocadlo, K.A. Stubbs, Modifying the phenyl group of PUGNAc: reactivity tuning to deliver selective inhibitors for N-acetyl-D-glucosaminidases, *Org. Biomol. Chem.* 14 (2016) 3193–3197.
- [27] D. Beer, J.-L. Maloisel, D.M. Rast, A. Vasella, Synthesis of 2-Acetamido-2-deoxy-D-gluconohydroxymalactone- and chitobionhydroxymalactone-derived N-phenylcarbamates, potential inhibitors of β -N-acetylglucosaminidase, *Helv. Chim. Acta* 73 (1990) 1918–1922.
- [28] H. Mohan, A. Vasella, An improved synthesis of 2-Acetamido-2-deoxy-D-gluconohydroxymalactone (PUGNAc), A strong inhibitor of β -N-acetylglucosaminidases, *Helv. Chim. Acta* 83 (2000) 114–118.
- [29] D.R. Wolk, A. Vasella, F. Schweikart, M.G. Peter, Synthesis and enzyme-inhibition studies of phenylsemicarbazones derived from D-glucono-1,5-lactone and 2-acetamido-2-deoxy-D-glucono-1,5-lactone, *Helv. Chim. Acta* 75 (1992) 323–334.
- [30] D. Chaplin, D.H.G. Crout, S. Bornemann, D.W. Hutchinson, R. Khan, Conversion of 2-acetamido-2-deoxy- β -D-galactopyranose (N-acetylglucosamine) into 2-acetamido-2-deoxy- β -D-galactopyranose (N-acetylgalactosamine) using a biotransformation to generate a selectively deprotected substrate for S_N2 inversion, *J. Chem. Soc., Perkin Trans. 1* (1992) 235–237.
- [31] K.P. Ravindranathan Kartha, B. Mukhopadhyay, R.A. Field, Practical de-O-acylation reactions promoted by molecular sieves, *Carbohydr. Res.* 339 (2004) 729–732.
- [32] A. Bax, M.F. Summers, Proton and carbon-13 assignments from sensitivity-enhanced detection of heteronuclear multiple-bond connectivity by 2D multiple quantum NMR, *J. Am. Chem. Soc.* 108 (1986) 2093–2094.
- [33] C.M. Thiele, K. Petzold, J. Schleucher, EASY ROESY: reliable cross-peak integration in adiabatic symmetrized ROESY, *Chem. Eur. J.* 15 (2009) 585–588.
- [34] S.A. Goff, L.P. Casson, A.L. Goldberg, Heat shock regulatory gene htpR influences rates of protein degradation and expression of the lon gene in *Escherichia coli*, *Proc. Natl. Acad. Sci. Unit. States Am.* 81 (1984) 6647.
- [35] V. Tsilibaris, G. Maenhaut-Michel, L. Van Melderen, Biological roles of the Lon ATP-dependent protease, *Res. Microbiol.* 157 (2006) 701–713.
- [36] S. Luo, M. McNeill, T.G. Myers, R.J. Hohman, R.L. Levine, Lon protease promotes survival of *Escherichia coli* during anaerobic glucose starvation, *Arch. Microbiol.* 189 (2008) 181–185.
- [37] L. Wells, Y. Gao, J.A. Mahoney, K. Vosseller, C. Chen, A. Rosen, G.W. Hart, Dynamic O-glycosylation of nuclear and cytosolic proteins: further characterization of the nucleocytoplasmic β -N-acetylglucosaminidase, O-GlcNAcase, *J. Biol. Chem.* 277 (2002) 1755–1761.
- [38] C. Butkinaree, W.D. Cheung, S. Park, K. Park, M. Barber, G.W. Hart, Characterization of β -N-acetylglucosaminidase cleavage by caspase-3 during apoptosis*, *J. Biol. Chem.* 283 (2008) 23557–23566.
- [39] S. Wadhawan, S. Gautam, Rescue of *Escherichia coli* cells from UV-induced death and filamentation by caspase-3 inhibitor, *Int. Microbiol.* 22 (2019) 369–376.
- [40] K.W. Bayles, Bacterial programmed cell death: making sense of a paradox, *Nat. Rev. Microbiol.* 12 (2014) 63–69.
- [41] F. Baneyx, M. Mujacic, Recombinant protein folding and misfolding in *Escherichia coli*, *Nat. Biotechnol.* 22 (2004) 1399–1408.
- [42] F.D. Schramm, K. Schroeder, K. Jonas, Protein aggregation in bacteria, *FEMS (Fed. Eur. Microbiol. Soc.) Microbiol. Rev.* 44 (2020) 54–72.
- [43] D.M. Francis, R. Page, Strategies to optimize protein expression in *E. coli*, *Current Protocols in Protein Science* 61 (2010), 5.24.21–5.24.29.
- [44] N.L. Elsen, S.B. Patel, R.E. Ford, D.L. Hall, F. Hess, H. Kandula, M. Kornienko, J. Reid, H. Selnick, J.M. Shipman, S. Sharma, K.J. Lumb, S.M. Soisson, D.J. Klein, Insights into activity and inhibition from the crystal structure of human O-GlcNAcase, *Nat. Chem. Biol.* 13 (2017) 613–615.
- [45] M. Dixon, The determination of enzyme inhibitor constants, *Biochem. J.* 55 (1953) 170–171.
- [46] A. Cornish-Bowden, A simple graphical method for determining the inhibition constants of mixed, uncompetitive and non-competitive inhibitors, *Biochem. J.* 137 (1974) 143–144.
- [47] E.J. Kim, D.O. Kang, D.C. Love, J.A. Hanover, Enzymatic characterization of O-GlcNAcase isoforms using a fluorogenic GlcNAc substrate, *Carbohydr. Res.* 341 (2006) 971–982.
- [48] Schrödinger Release 2018-4, Schrödinger, LLC, New York, NY, 2018.
- [49] U. Ryde, P. Söderhjelm, Ligand-binding affinity estimates supported by quantum-mechanical methods, *Chem. Rev.* 116 (2016) 5520–5566.
- [50] K.E. Tsitsonou, J.M. Hayes, M. Keramioti, M. Mamais, N.G. Oikonomakos, A. Kato, D.D. Leonidas, S.E. Zographos, Sourcing the affinity of flavonoids for the glycogen phosphorylase inhibitor site via crystallography, kinetics and QM/MM-PBSA binding studies: comparison of chrysin and flavopiridol, *Food Chem. Toxicol.* 61 (2013) 14–27.
- [51] B.A. Chetter, E. Kyriakis, D. Barr, A.G. Karra, E. Katsidou, S.M. Koulas, V.T. Skamnaki, T.J. Snape, A.-M.G. Psarra, D.D. Leonidas, J.M. Hayes, Synthetic flavonoid derivatives targeting the glycogen phosphorylase inhibitor site: QM/MM-PBSA motivated synthesis of substituted 5,7-dihydroxyflavones, crystallography, *in vitro* kinetics and *ex-vivo* cellular experiments reveal novel potent inhibitors, *Bioorg. Chem.* 102 (2020) 104003.
- [52] C.D. Sherrill, T. Takatani, E.G. Hohenstein, An assessment of theoretical methods for nonbonded interactions: comparison to complete basis set limit coupled-cluster potential energy curves for the benzene dimer, the methane dimer, Benzene–Methane, and Benzene–H₂S, *J. Phys. Chem.* 113 (2009) 10146–10159.
- [53] Y. Zhao, D.G. Truhlar, The M06 suite of density functionals for main group thermochemistry, thermochemical kinetics, noncovalent interactions, excited states, and transition elements: two new functionals and systematic testing of four M06-class functionals and 12 other functionals, *Theor. Chem. Accounts* 120 (2008) 215–241.
- [54] E.G. Hohenstein, S.T. Chill, C.D. Sherrill, Assessment of the performance of the M05–2X and M06–2X exchange-correlation functionals for noncovalent interactions in biomolecules, *J. Chem. Theor. Comput.* 4 (2008) 1996–2000.
- [55] S. Manta, A. Xipinitou, C. Kiritis, A.L. Kantsadi, J.M. Hayes, V.T. Skamnaki, C. Lamprakis, M. Kontou, P. Zoumpoulakis, S.E. Zographos, D.D. Leonidas, D. Komiotis, 3'-Axial CH₂OH substitution on glucopyranose does not increase glycogen phosphorylase inhibitory potency. QM/MM-PBSA calculations suggest why, *Chem. Biol. Drug Des.* 79 (2012) 663–673.
- [56] M.O. Sinnokrot, C.D. Sherrill, Substituent effects in π - π Interactions: sandwich and T-shaped configurations, *J. Am. Chem. Soc.* 126 (2004) 7690–7697.
- [57] Y. Zhao, J. Li, H. Gu, D. Wei, Y.-c. Xu, W. Fu, Z. Yu, Conformational preferences of π - π stacking between ligand and protein, analysis derived from crystal structure data geometric preference of π - π interaction, *Interdiscipl. Sci. Comput. Life Sci.* 7 (2015) 211–220.
- [58] A.L. Ringer, M.O. Sinnokrot, R.P. Lively, C.D. Sherrill, The effect of multiple

- substituents on sandwich and T-shaped π - π interactions, *Chem. Eur. J.* 12 (2006) 3821–3828.
- [59] F.-Y. Lin, A.D. MacKerell, Do halogen–hydrogen bond donor interactions dominate the favorable contribution of halogens to ligand–protein binding? *J. Phys. Chem. B* 121 (2017) 6813–6821.
- [60] D. Barr, E. Szennyés, É. Bokor, Z.H. Al-Oanzi, C. Moffatt, S. Kun, T. Docsa, Á. Sipos, M.P. Davies, R.T. Mathomes, T.J. Snape, L. Agius, L. Somsák, J.M. Hayes, Identification of C- β -D-Glucopyranosyl azole-type inhibitors of glycogen phosphorylase that reduce glycogenolysis in hepatocytes: *in silico* design, synthesis, *in vitro* kinetics, and *ex vivo* studies, *ACS Chem. Biol.* 14 (2019) 1460–1470.
- [61] M.N. Aboul-Enein, A.A. El-Azzouny, M.I. Attia, Y.A. Maklad, K.M. Amin, M. Abdel-Rehim, M.F. El-Behairy, Design and synthesis of novel stiripentol analogues as potential anticonvulsants, *Eur. J. Med. Chem.* 47 (2012) 360–369.
- [62] M.S. Macauley, K.A. Stubbs, D.J. Vocadlo, O-GlcNAcase catalyzes cleavage of thioglycosides without general acid catalysis, *J. Am. Chem. Soc.* 127 (2005) 17202–17203.
- [63] A. Froger, J.E. Hall, Transformation of plasmid DNA into *E. coli* using the heat shock method, *JoVE* (2007) 253.
- [64] M.M. Bradford, A rapid and sensitive method for the quantitation of microgram quantities of protein utilizing the principle of protein–dye binding, *Anal. Biochem.* 72 (1976) 248–254.
- [65] W.W. Focke, I. van der Westhuizen, N. Musee, M.T. Loots, Kinetic interpretation of log-logistic dose–time response curves, *Sci. Rep.* 7 (2017) 2234.
- [66] A.M. Morris, R.G. Finke, α -Synuclein aggregation variable temperature and variable pH kinetic data: a re-analysis using the Finke–Watzky 2-step model of nucleation and autocatalytic growth, *Biophys. Chem.* 140 (2009) 9–15.
- [67] C.R. Søndergaard, M.H.M. Olsson, M. Rostkowski, J.H. Jensen, Improved treatment of ligands and coupling effects in empirical calculation and rationalization of pK_a values, *J. Chem. Theor. Comput.* 7 (2011) 2284–2295.
- [68] G.A. Kaminski, R.A. Friesner, J. Tirado-Rives, W.L. Jorgensen, Evaluation and reparametrization of the OPLS-AA force field for proteins via comparison with accurate quantum chemical calculations on peptides, *J. Phys. Chem. B* 105 (2001) 6474–6487.
- [69] E. Harder, W. Damm, J. Maple, C. Wu, M. Reboul, J.Y. Xiang, L. Wang, D. Luyuan, M.K. Dahlgren, J.L. Knight, J.W. Kaus, D.S. Cerutti, G. Krilov, W.L. Jorgensen, R. Abel, R.A. Friesner, OPLS3: a force field providing broad coverage of drug-like small molecules and proteins, *J. Chem. Theor. Comput.* 12 (2016) 281–296.
- [70] J. Li, R. Abel, K. Zhu, Y. Cao, S. Zhao, R.A. Friesner, The VSGB 2.0 model: a next generation energy model for high resolution protein structure modeling, *Proteins: Struct. Funct. Bioinf.* 79 (2011) 2794–2812.
- [71] M.M. Francl, W.J. Pietro, W.J. Hehre, J.S. Binkley, M.S. Gordon, D.J. DeFrees, J.A. Pople, Self-consistent molecular orbital methods. XXIII. A polarization-type basis set for second-row elements, *J. Chem. Phys.* 77 (1982) 3654–3665.
- [72] W.J. Hehre, R. Ditchfield, J.A. Pople, Self-consistent molecular orbital methods. XII. Further extensions of Gaussian–type basis sets for use in molecular orbital studies of organic molecules, *J. Chem. Phys.* 56 (1972) 2257–2261.
- [73] R.B. Murphy, D.M. Philipp, R.A. Friesner, A mixed quantum mechanics/molecular mechanics (QM/MM) method for large-scale modeling of chemistry in protein environments, *J. Comput. Chem.* 21 (2000) 1442–1457.
- [74] B. Marten, K. Kim, C. Cortis, R.A. Friesner, R.B. Murphy, M.N. Ringnalda, D. Sitkoff, B. Honig, New model for calculation of solvation free Energies: correction of self-consistent reaction field continuum dielectric theory for short-range hydrogen-bonding effects, *J. Phys. Chem.* 100 (1996) 11775–11788.
- [75] S.F. Boys, F. Bernardi, The calculation of small molecular interactions by the differences of separate total energies. Some procedures with reduced errors, *Mol. Phys.* 19 (1970) 553–566.